Imaging Magnetization Structure and Dynamics in Ultrathin $Y_3Fe_5O_{12}$/Pt Bilayers with High Sensitivity Using the Time-Resolved Longitudinal Spin Seebeck Effect

Jason M. Bartell,[1] Colin L. Jermain,[1] Sriharsha V. Aradhya,[1] Jack T. Brangham,[2] Fengyuan Yang,[2] Daniel C. Ralph,[1,3] and Gregory D. Fuchs[1]

[1]*Cornell University, Ithaca, New York 14853, USA*
[2]*Department of Physics, The Ohio State University, Columbus, Ohio 43016, USA*
[3]*Kavli Institute at Cornell for Nanoscale Science, Ithaca, New York 14853, USA*

(Received 17 January 2017; published 6 April 2017)

We demonstrate an instrument for time-resolved magnetic imaging that is highly sensitive to the in-plane magnetization state and dynamics of thin-film bilayers of yttrium iron garnet $[Y_3Fe_5O_{12}(\mathrm{YIG})]$/Pt: the time-resolved longitudinal spin Seebeck (TRLSSE) effect microscope. We detect the local in-plane magnetic orientation within the YIG by focusing a picosecond laser to generate thermally driven spin current from the YIG into the Pt by the spin Seebeck effect and then use the inverse spin Hall effect in the Pt to transduce this spin current to an output voltage. To establish the time resolution of TRLSSE, we show that pulsed optical heating of patterned YIG (20 nm)/Pt(6 nm)/Ru(2 nm) wires generates a magnetization-dependent voltage pulse of less than 100 ps. We demonstrate TRLSSE microscopy to image both static magnetic structure and gigahertz-frequency magnetic resonance dynamics with submicron spatial resolution and a sensitivity to magnetic orientation below $0.3°/\sqrt{Hz}$ in ultrathin YIG.

DOI: 10.1103/PhysRevApplied.7.044004

I. INTRODUCTION

Ultrathin bilayers of the magnetic insulator $Y_3Fe_5O_{12}$ (YIG) interfaced with a heavy nonmagnetic metal such at Pt are being intensely studied for the development of high-efficiency magnetic memory and logic devices operated by spin-orbit torque [1,2], for magnon generation and propagation [3–5], and as a model system for understanding spin-current generation by the longitudinal spin Seebeck effect (LSSE) and spin pumping [6–9]. For all of these research areas, it is useful to have a high-sensitivity and local probe of magnetization dynamics in the YIG layer, especially for the ultrathin films required in many devices. This has proven challenging, and although magneto-optical techniques such as Brillouin light scattering and the magneto-optical Kerr effect have proven valuable [3,10–14], they have not enabled direct time-resolved imaging of magnetic precession or direct imaging of in-plane magnetization of ultrathin YIG films (20 nm and below). An alternative approach that enables in-plane imaging of YIG/Pt bilayer devices was demonstrated by Weiler *et al.* [15]. In that work, the authors use laser heating to image the in-plane magnetic structure of YIG but not its dynamics. Here we extend the approach into the time domain to perform high-sensitivity imaging of the in-plane magnetic orientation ($<0.3°/\sqrt{Hz}$) with submicron spatial resolution and sub-100-ps temporal resolution. Using TRLSSE microscopy, we can observe, for example, that the resonance field in ultrathin YIG films can vary by up to 30 Oe within micron-scale regions of a YIG/Pt device. Our results demonstrate that TRLSSE microscopy is a powerful tool to characterize static and dynamic magnetic properties in ultrathin YIG.

The principle behind the TRLSSE microscope shown schematically in Fig. 1 is the generation and detection of a thermally generated local spin current [16]. For the case of YIG/Pt, a local thermal gradient perpendicular to the film plane is generated by laser heating of Pt. The gradient creates a thermally induced spin current that is proportional to the local magnetization [17–19]. The spin current that flows into the Pt is detected with the ISHE [20,21] in which spin-orbit

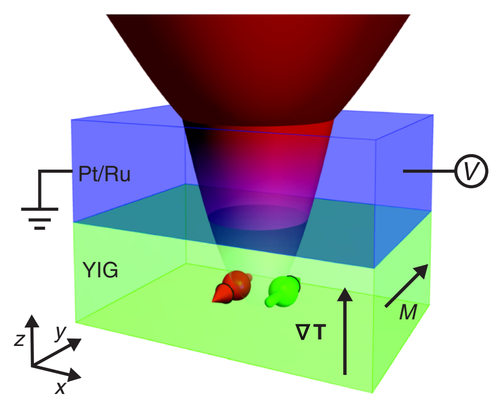

FIG. 1. Schematic of our TRLSSE measurement. A 780-nm 3-ps pulsed laser focused to a 0.606-μm-diameter spot is used to heat a YIG (20 nm)/Pt(6 nm)/Ru(2 nm) film. The heating from the laser creates a temperature gradient $\mathbf{\nabla T}_z$. The pulsed heating drives a pulsed magnon flux J_s from the YIG into the Pt where it is transduced into a pulsed voltage via the ISHE.

coupling leads to a spin-dependent transverse electric field. For this work, the resulting voltage can be described as [17,19] $V_{\mathrm{LSSE}} \propto -\xi_{\mathrm{SH}} S[\mathbf{M}(\boldsymbol{x},t)/M_s] \times \boldsymbol{\nabla}\mathbf{T}(\boldsymbol{x},t)$, where ξ_{SH} is the spin Hall efficiency, S is the spin Seebeck coefficient, $\mathbf{M}$ is the local magnetization, M_s is the saturation magnetization, and $\boldsymbol{\nabla}\mathbf{T}$ is the thermal gradient. The LSSE has been attributed to both thermal gradients across the thickness of YIG and to interfacial temperature differences between YIG and Pt [17–19,22,23]. Our experiment cannot definitively distinguish between these two mechanisms. Thus, here we discuss only $\boldsymbol{\nabla}\mathbf{T}$ as the single quantity for simplicity and for consistency with our prior work using the anomalous Nernst effect; however, this question requires further study. V_{LSSE} is a readout of the local magnetization m_y because the electric field is generated in response to the spatially local z component of the thermal gradient $\boldsymbol{\nabla}\mathbf{T}_z$ (coordinates as defined in Fig. 1) [15,24].

To extend LSSE imaging into the time domain, we use picosecond laser heating to stroboscopically sample magnetization. We have previously shown [25] in metallic ferromagnets that picosecond heating can be used for stroboscopic magnetic microscopy using the time-resolved anomalous Nernst effect (TRANE). In TRANE microscopy, the temporal resolution is set by the excitation and decay of a thermal gradient within a single material that both absorbs the heat from the laser pulse and produces a TRANE voltage from internal spin-orbit interactions [26,27]. In the LSSE, however, the time scale of spin-current generation can depend on both the time scale of the thermal gradient and the time scale of energy transfer between the phonons and magnons. Recent experiments indicate that in the qausistatic regime, the magnon-phonon relaxation rate may play a dominant role [28–31]. Using picosecond heating and time-resolved electrical detection to move beyond the quasistatic regime, we show a TRLSSE in agreement with a recent all-optical experiment [22].

II. DESCRIPTION OF EXPERIMENT

We grow our samples using off-axis sputtering onto (110)-oriented gadolinium gallium garnet [$Gd_3Ga_5O_{12}$ (GGG)] [32–34] followed by *ex situ* deposition of 6 nm of Pt with a 2-nm Ru capping layer. Photolithography and ion milling are used to pattern wires and contacts for wire bonding. We present measurements of a $2 \times 10\ \mu\mathrm{m}^2$ wire and a $4 \times 10\ \mu\mathrm{m}^2$ wire with dc resistances of 296 and 111 Ω, respectively. In this room-temperature study, we neglect the potential anomalous Nernst effect of interfacial Pt with induced magnetization [35,36], and we neglect a possible photospin voltaic effect [37], neither of which can be distinguished from the TRLSSE in the presented measurements.

Our TRLSSE measurement consists of pulsed-laser heating and homodyne electrical detection as shown in Fig. 2(a). We use a Ti:sapphire laser pulse to locally heat the sample with 3-ps pulses of 780-nm light at a repetition rate of 25.5 MHz. The electrical signal produced at the sample is the sum of the LSSE-dependent voltage

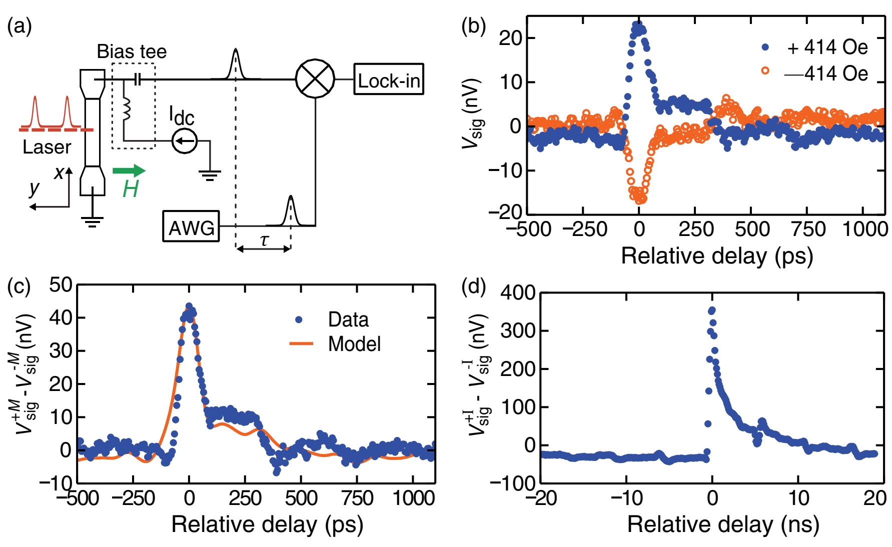

FIG. 2. (a) Schematic of the LSSE detection circuit used for time-resolved voltage measurements. (b) Time-domain measurement of the LSSE-generated voltage in the 2-μm-wide wire. The time-varying LSSE signal is measured by electrically mixing the pulsed-laser-generated voltage with a 100-ps voltage pulse from the AWG. Comparing measurements of the YIG at +414 Oe (filled blue circles) and −414 Oe (open orange circles) shows that the signal depends on the orientation of the magnetic moment. Here the dc level noise is removed. The data are acquired with a lock-in time constant of 500 ms and integration time of 2 s per point. (c) The solid blue circles show the difference between the two curves in (b). The orange line is a model normalized by the data amplitude of the signal determined by numerically convolving the calculated thermal gradient with the measured mixing pulse. (d) Difference signal of the temperature-dependent voltage V_J measured using $+/-0.5$ mA and a 600-ps mixing pulse. In (b)–(d), we report the voltage as detected at the lock-in after passing through the rf mixer, not the LSSE signal at the sample itself.

$V_{\mathrm{LSSE}}(\nabla\mathbf{T}_z, \mathbf{M})$ and a voltage $V_J(\Delta T, J)$, which is generated when a current density J passes through the local region of Pt with increased resistance due to laser heating [38]. To reject noise and recover the signal of the resulting electrical pulses, we use a time-domain homodyne technique in which we mix the $V_{\mathrm{LSSE}}+V_J$ pulse train with a synchronized reference pulse train V_{mix} in a broadband (0.1–12 GHz) electrical mixer. The mixer output is the convolution of the two pulse trains given by [38]

$$V_{\mathrm{sig}}(\boldsymbol{x},\tau) = K\int_0^{\Gamma}(V_{\mathrm{LSSE}}(\nabla\mathbf{T}_z(\boldsymbol{x},t),\mathbf{M}(\boldsymbol{x},t)) + V_J(\Delta T(\boldsymbol{x},t),J(\boldsymbol{x},t)))V_{\mathrm{mix}}(\tau-t)dt, \quad (1)$$

where $\boldsymbol{x}(x,y)$ is the laser spot position in the sample plane, Γ is the period of the laser pulses, K is the transfer coefficient, and τ is the relative delay. A relative delay of zero corresponds to the maximum of both pulse trains arriving at the mixer simultaneously.

We study the time scale of the LSSE signal generated by a picosecond pulse by measuring V_{sig} as a function of mixer delay τ. Figure 2(b) shows the result of this measurement using a 100-ps mixing pulse reference V_{mix} at a saturating magnetic field H perpendicular to the wire at $H = +414$ and -414 Oe, respectively. In Fig. 2(c), we plot the difference between these two voltage traces to reject nonmagnetic contributions. We find that the full width at half maximum (FWHM) is 100 ± 10 ps, which is followed by electrical oscillations that we attribute to nonidealities in the detection circuit (see the Supplemental Material [39] for further discussion). Because the duration of the magnetic component of V_{sig} is experimentally indistinguishable from the FWHM of V_{mix}, we conclude that 100 ps is an experimental upper bound for the TRLSSE signal duration.

To calibrate the local change in the Pt temperature ΔT_{Pt} due to picosecond heating and to quantify the rate of thermal relaxation, we measure V_J in the presence of a dc current, which uses the local Pt resistivity as an ultrafast thermometer. Figure 2(d) shows V_J as a function of mixer delay $V_J(\tau) = V_{\mathrm{sig}}(\tau, J = 4.2\ \mathrm{MA/cm^2}) - V_{\mathrm{sig}}(\tau, J = -4.2\ \mathrm{MA/cm^2})$ for applied currents of ±0.5 mA. $V_J(\tau)$ is proportional to ΔT_{Pt} through V_J, but it is not proportional to either the magnetic state of the sample or $\nabla\mathbf{T}_z$. We observe that V_J relaxes to zero faster than the laser repetition period, indicating that the sample thermally recovers between pulses. To quantitatively consider the spatiotemporal thermal evolution, we perform a time-domain finite-element (TDFE) calculation of focused-laser heating in the wire. Additional details are available in the Supplemental Material [39], and see Ref. [25] for a lengthier discussion of the procedure. The comparison of the spatiotemporal profile of the calculation and the known temperature dependence of resistivity enable us to calibrate the spatiotemporal temperature rise due to laser heating. We find that the peak film temperature changes by approximately 50 K in the platinum and approximately 10 K in the YIG for a laser fluence of 5.8 $\mathrm{mJ/cm^2}$, which is the maximum for the presented measurements [40–44]. Note that we assume all laser heating is mediated by optical absorption in Pt because YIG and GGG are transparent at 780 nm [45,46]. The TDFE calculation reveals that in agreement with experiment, $\nabla\mathbf{T}_z$ across the YIG thickness decays more quickly than the full thermal relaxation of the Pt back to the ambient temperature (e.g., $\Delta T_{\mathrm{Pt}} = 0$). This difference in time scales between $\nabla\mathbf{T}_z$ and ΔT_{Pt} is important because the magnetic signal in our experiment is sensitive to only $\nabla\mathbf{T}_z(t)$ not $\Delta T_{\mathrm{Pt}}\ (t)$ of the Pt.

III. STROBOSCOPIC MEASUREMENT OF FERROMAGNETIC RESONANCE

The sub-100-ps spin-current lifetime in our experiment is short enough that the TRLSSE is useful for stroboscopic measurements of resonant YIG magnetization dynamics. To confirm this idea, we use TRLSSE microscopy to measure ferromagnetic resonance (FMR) by driving a gigahertz-frequency ac current into the Pt, which generates magnetic torques on YIG from both the Oersted magnetic field and from spin currents generated by the spin Hall effect [47–49]. The current is generated with an arbitrary waveform generator (AWG) that is phase locked to the laser repetition rate and coupled to the YIG/Pt device through a circulator [see schematic in Fig. 3(a)]. Synchronizing the ac current and the laser repetition rate ensures a constant but controllable phase between the precessing magnetization and the sensing heat pulse for a given driving frequency and magnetic field. In our FMR measurements, we fix $\tau = 0$ and align the wire axis parallel to the external magnetic field. In this configuration, the TRLSSE signal is stroboscopically sensitive to the magnetic projection m_y at a particular phase of the magnetic precession about the x axis. In addition to V_{LSSE}, V_{sig} contains a contribution from V_J that is proportional to the local ac current amplitude and phase [38]. We separate the magnetic V_{LSSE} from the nonmagnetic V_J by measuring V_{sig} with a lock-in amplifier referenced to a 383-Hz 7.6-Oe rms modulation of the external magnetic field. Figure 3(b) shows LSSE FMR spectra as a function of field excited using a 1.2 ± 0.3- and 1.4 ± 0.4-mA ac current at 4.1 and 4.9 GHz, respectively. In the limit that the modulation magnetic field is small compared to the FMR linewidth, we can interpret the resulting signal V_{mod} as a derivative signal that contains a linear combination of the real and imaginary parts of the dynamic susceptibility χ, $V_{\mathrm{mod}}(H) \propto (d\chi'/dH)\sin(\theta) + (d\chi''/dH)\cos(\theta)$. This relation is used to fit the FMR spectra to extract the amplitude, phase, linewidth, and resonant field. For more details on fitting, see Refs. [25,38]. To demonstrate that the TRLSSE microscope is a

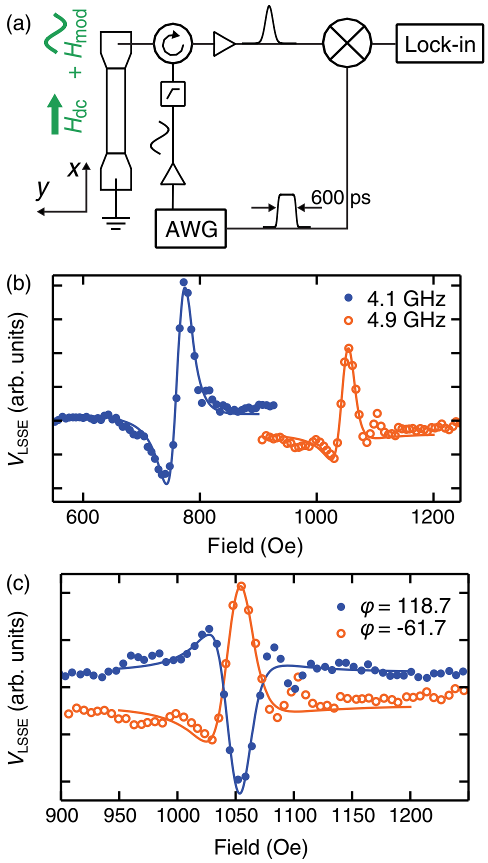

FIG. 3. Stroboscopic detection of ferromagnetic resonance. (a) Schematic of measurement circuit for detection of magnetization dynamics in the 2-μm-wide wire. (b) TRLSSE-detected FMR for 4.1-GHz (blue closed circles) and 4.9-GHz (orange open circles) excitation. The solid lines are a fit to the data using a modified Lorentzian function. (c) Demonstration of stroboscopic FMR detection in which we measure the response of the YIG driven at phases that differ by 180°. The data are acquired with a lock-in time constant of 1 s and integration time of 5 s per point.

phase-sensitive stroboscope, we rotate the phase of the microwave current by 180° and remeasure FMR. As expected, inverting the phase of the drive inverts the phase of the FMR line shape [Fig. 3(c)].

IV. CHARACTERIZATION OF SENSITIVITY

Next, we quantify the sensitivity of TRLSSE microscopy for our ultrathin YIG/Pt samples. Figure 4 shows representative TRLSSE measurements of the YIG magnetization versus magnetic field perpendicular to the wire at several optical powers. In this geometry, the positive and negative saturation values of V_{LSSE} quantify the full range of magnetization $+M$ to $-M$. Then, using the standard deviation of the noise in the TRLSSE voltage σ_{LSSE}, we can quantify the angular sensitivity noise floor assuming small-angle magnetic deviations from the wire axis, such as for stroboscopic FMR measurements. The

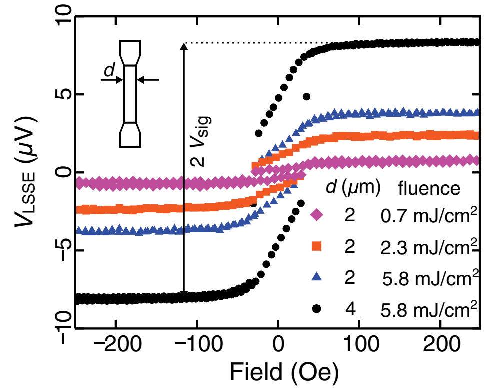

FIG. 4. Measurement of YIG magnetization with LSSE measuring V_{LSSE} versus external magnetic field for different laser powers and wire widths. For these curves, a dc background is subtracted. The inset shows the wire geometry. We define the signal size to be one-half of the difference in voltage when the magnetization is saturated in opposing directions. The data are acquired with a lock-in time constant of 500 ms and integration time of 2 s per point.

sensitivity is calculated using [25] $\theta_{\min} = \{\sigma_{\mathrm{LSSE}}/[\sin(\theta_o)(V_{\mathrm{LSSE}}^{\max} - V_{\mathrm{LSSE}}^{\min})/2]\}\sqrt{\mathrm{TC}}$, where TC is the lock-in time constant. We find a sensitivity of $0.3^{\circ}/\sqrt{\mathrm{Hz}}$ for an optical power of 0.6 mW corresponding to a laser fluence of $5.8\ \mathrm{mJ/cm^2}$. It is important to note that the sensitivity is sample dependent through both sample geometry and the impedance match with the detection circuit [25].

The interface quality of the sample plays a key role in determining the sensitivity. As spin current diffuses into the platinum, it is subject to loss at the interface. A good indication of interfacial spin transparency is the spin Hall magnetoresistance (SMR) [50,51], which is sensitive to the spin-mixing conductance at the interface. For the data presented here, the devices show a SMR of 0.063%, which is the largest value by a factor of 2 from the other devices we pattern. This is consistent with a number of recent SMR reports [50–54], and we expect the high SMR value indicates strong spin transparency at the YIG/Pt interface. We also study YIG/Pt samples with no measurable SMR, which we expect to have a significantly reduced LSSE-induced ISHE voltage. We find that the TRLSSE signal in these devices is approximately an order of magnitude lower for the same laser fluence. Additional details are in the Supplemental Material [39].

V. IMAGING STATIC AND DYNAMIC MAGNETIZATION

Having placed upper bounds on the time resolution and quantified the sensitivity, next we demonstrate the application of TRLSSE microscopy for imaging of static magnetization. We acquire images by scanning the laser focus and making a point-by-point measurement of the TRLSSE voltage and reflected light. Figures 5(a) and 5(b)

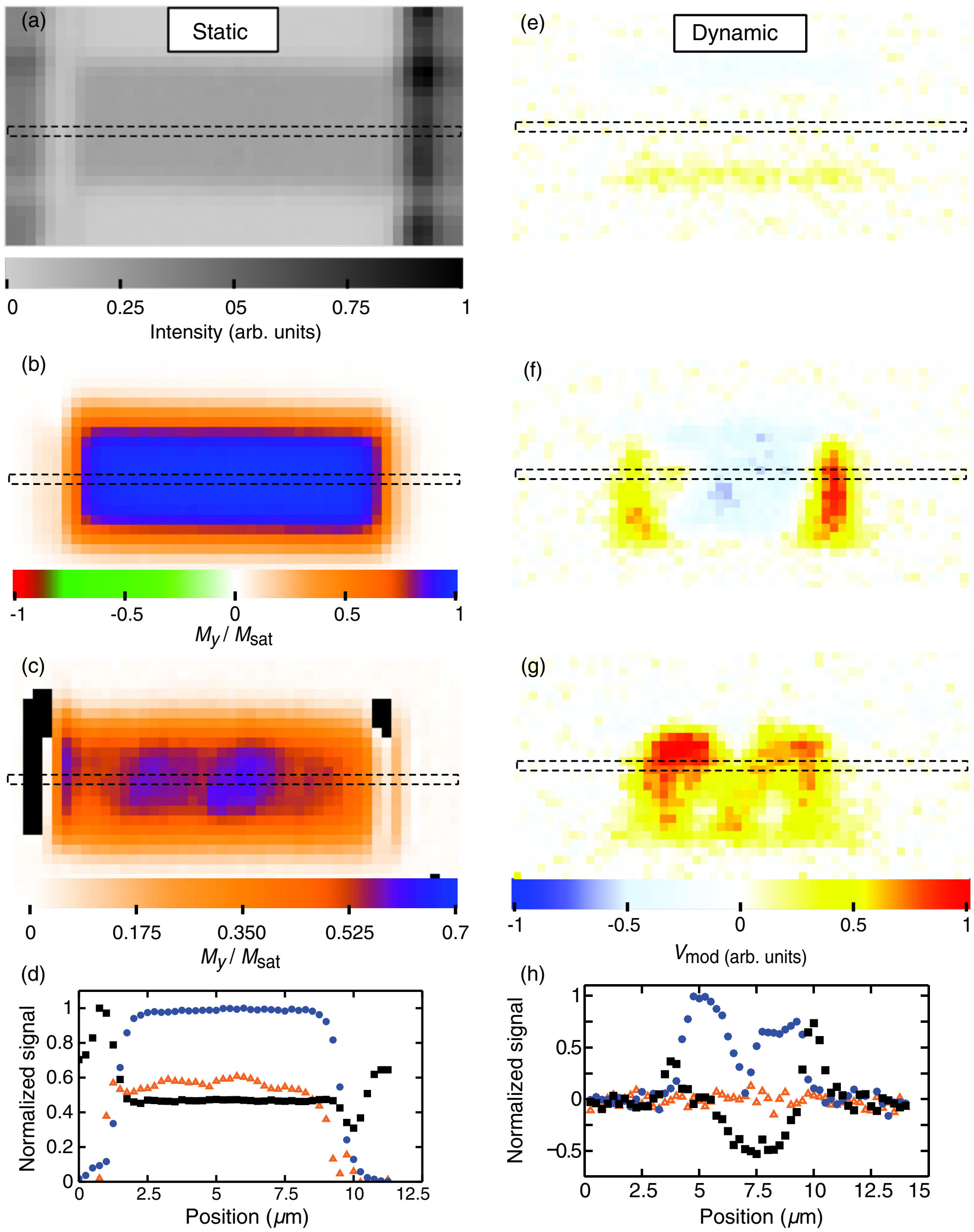

FIG. 5. Images of the 4-μm-wide YIG/Pt wire. (a) Reflected light image of the YIG/Pt wire measured with a photodiode at the same time as the LSSE voltage. (b) Background-subtracted LSSE voltage at saturated magnetization and (c) remnant magnetization at 4 Oe after saturation. (d) Line cuts of the 2D scans. The normalized reflection signal is shown with black squares, blue circles represent the saturated magnetization, and the orange triangles represent the magnetization of the remnant state. Note that in the line cuts, the low-field line cut is normalized with respect to the saturation magnetization. The right side of the figure represents the raw images of the 4-μm wire at different fields around the resonance: (e) 896 Oe, (f) 1007 Oe, (g) 1025 Oe. Images (e)–(g) share the same color scale. Line cuts of the images are shown in (h); black squares, blue circles, and orange triangles correspond to the boxed regions of (e), (f), and (g), respectively. For (e)–(g), the data are acquired with a lock-in time constant of 200 ms and an integration time of 2 s.

show a reflected light image and saturated LSSE image, respectively, for a 4-μm-wide YIG/Pt device. In the reflection image, we see the structure of the wire and the contact pads at both ends. We acquire the TRLSSE image at $H = -405$ Oe and shift the background level for clarity of the color scale. No other image processing is performed. We observe a uniform magnetization state of the YIG/Pt device, as expected from the previously presented magnetic hysteresis measurements (Fig. 4). When we reduce the field to near zero ($H = 4$ Oe) and reimage the wire [Fig. 5(c)], magnetic texture is revealed that indicates nonuniform canting of the device magnetization. To more clearly show the variation in contrast between images, we plot line cuts of Figs. 5(a)–5(c) in Fig. 5(d). Despite the inhomogeneous remanence that is evident in Fig. 5(c), we are not able to observe domains with oppositely aligned magnetization, possibly because once a reversal domain is nucleated, the domain wall propagates without strong pinning.

Without a 180° domain wall, the spatial resolution of TRLSSE cannot be directly evaluated. Nevertheless, we use the reflected light image and TDFE simulations to study the possibility that lateral thermal spreading degrades the resolution. To approximate the lateral point-spread function of the laser, we fit a scan of the wire step edge to a Gaussian point-spread function. This yields a spot FWHM of 0.606 μm. The calculations of the heating indicate that the thermal gradient does not spread laterally in the Pt; thus, we expect that the resolution of the TRLSSE is the same as the diffraction-limited optical resolution in this experiment.

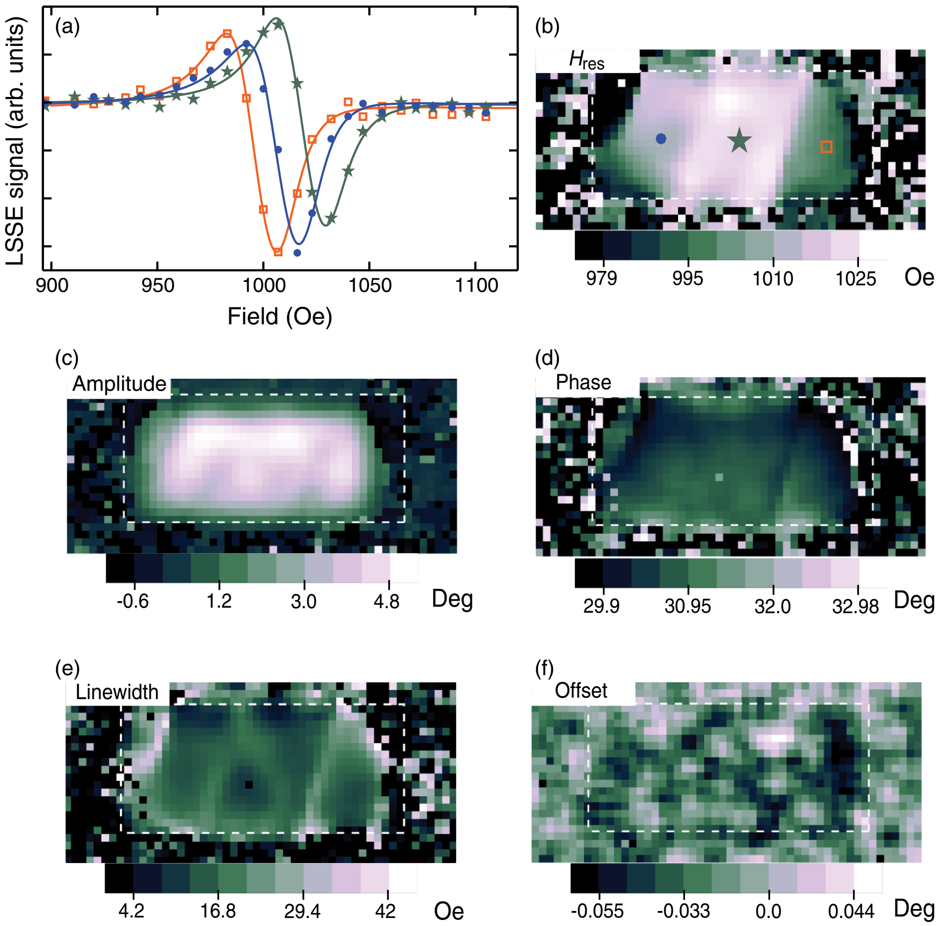

FIG. 6. Spatial maps of FMR fitting parameters for the 4-μm-wide wire. (a) Traces are the pixel values of three points on the sample as a function of magnetic field. (b)–(f) Spatial maps of the FMR fitting parameters made by fitting of the FMR curves at each pixel in the sequence of images measured with LSSE. Before fitting, we correct for image-to-image offset and use a 3×3 pixel moving average to smooth the data. (b) Resonance field: the symbols mark the pixels corresponding to the FMR spectra shown in (a). (c) Resonance amplitude, (d) resonance phase, (e) resonance linewidth (f) offset used in the fit.

We now demonstrate that TRLSSE microscopy has the sensitivity to image dynamic magnetization in the 4-μm YIG/Pt device, which provides quantitative and spatially localized information about the dynamical properties of ultrathin YIG materials. As we describe above, for FMR characterization we orient the external magnetic field parallel to the wire axis and drive a 1.2 ± 0.1-mA 4.9-GHz current into the wire. We image dynamical magnetization at a series of magnetic fields near the resonance field from $H = 896$ to 1105 Oe and plot a selection of the unprocessed images in Figs. 5(e)–5(g). The data show that at H far from resonance [Fig. 5(e)] where precession amplitudes are tiny, the TRLSSE signal at the center of the wire is well below the detection noise floor. There is a small current-induced nonmagnetic signal artifact at the edges of the wire, which we discuss further in the Supplemental Material [39]. For H near the resonant field H_{res}, the device has a strong position-dependent TRLSSE response. To quantitatively analyze the data, images are corrected for background offset and sample drift before fitting a resonance field curve for each pixel. We plot a selection of curves from individual pixels in Fig. 6(a). We then construct a spatial map of each fitting parameter: H_{res}, relative phase, ϕ, amplitude, A, linewidth, ΔH, and offset, all of which are shown in Figs. 6(b)–6(f). We immediately notice spatial variation in these images that is qualitatively similar to the nonuniform magnetic remanence texture shown in Fig. 5(c). Together, these measurements confirm the presence of varying local magnetic anisotropy and quantify both static and dynamic magnetic properties in each region. The ability to quantitatively relate the spatial variation of static and dynamic properties in ultrathin YIG/Pt devices is an important capability of our microscope.

VI. CONCLUSION

In conclusion, we demonstrate sensitive and high-resolution TRLSSE microscopy of ultrathin YIG/Pt devices that we expect will prove useful for developing spintronic applications. Using picosecond heating, we demonstrate that TRLSSE microscopy is a sub-100-ps probe of ultrathin YIG/Pt device magnetization both for static magnetic configurations and for dynamical measurements at gigahertz frequencies. We demonstrate an angular sensitivity of $0.3^{\circ}/\sqrt{Hz}$, making it a sensitive experimental probe of ultrathin YIG magnetic orientation.

ACKNOWLEDGMENTS

We thank J. Kimling and D. G. Cahill for helpful comments on an early version of the manuscript and for providing the interface thermal resistance of YIG/Pt. This research is supported by the U.S. Air Force Office of Scientific Research under Contract No. FA9550-14-1-0243, by U.S. National Science Foundation under Grants No. DMR-1406333 and No. DMR-1507274, and through the Cornell Center for Materials Research (CCMR) (Grant No. DMR-1120296). This work makes use of the CCMR Shared Facilities and the Cornell NanoScale Facility, a member of the National Nanotechnology Coordinated Infrastructure, which is supported by the National Science Foundation (Grant No. ECCS-1542081).

[1] B. Behin-Aein, D. Datta, S. Salahuddin, and S. Datta, Proposal for an all-spin logic device with built-in memory, Nat. Nanotechnol. **5**, 266 (2010).

[2] K. Ganzhorn, S. Klingler, T. Wimmer, S. Geprägs, R. Gross, H. Huebl, and S. T. B. Goennenwein, Magnon-based logic in a multi-terminal YIG/Pt nanostructure, Appl. Phys. Lett. **109**, 022405 (2016).

[3] C. W. Sandweg, Y. Kajiwara, A. V. Chumak, A. A. Serga, V. I. Vasyuchka, M. B. Jungfleisch, E. Saitoh, and B. Hillebrands, Spin Pumping by Parametrically Excited Exchange Magnons, Phys. Rev. Lett. **106**, 216601 (2011).

[4] H. Kurebayashi, O. Dzyapko, V. E. Demidov, D. Fang, A. J. Ferguson, and S. O. Demokritov, Controlled enhancement of spin-current emission by three-magnon splitting, Nat. Mater. **10**, 660 (2011).

[5] P. Pirro, T. Brächer, A. V. Chumak, B. Lägel, C. Dubs, O. Surzhenko, P. Görnert, B. Leven, and B. Hillebrands, Spin-wave excitation and propagation in microstructured waveguides of yttrium iron garnet/Pt bilayers, Appl. Phys. Lett. **104**, 012402 (2014).

[6] K. Uchida, J. Xiao, H. Adachi, J. Ohe, S. Takahashi, J. Ieda, T. Ota, Y. Kajiwara, H. Umezawa, H. Kawai, G. E. W. Bauer, S. Maekawa, and E. Saitoh, Spin Seebeck insulator, Nat. Mater. **9**, 894 (2010).

[7] K. Uchida, H. Adachi, T. An, T. Ota, M. Toda, B. Hillebrands, S. Maekawa, and E. Saitoh, Long-range spin Seebeck effect and acoustic spin pumping, Nat. Mater. **10**, 737 (2011).

[8] G. E. W. Bauer, E. Saitoh, and B. J. van Wees, Spin caloritronics., Nat. Mater. **11**, 391 (2012).

[9] S. R. Boona, R. C. Myers, and J. P. Heremans, Spin caloritronics, Energy Environ. Sci. **7**, 885 (2014).

[10] V. E. Demidov, M. Evelt, V. Bessonov, S. O. Demokritov, J. L. Prieto, M. Muñoz, J. Ben Youssef, V. V. Naletov, G. de Loubens, O. Klein, M. Collet, P. Bortolotti, V. Cros, and A. Anane, Direct observation of dynamic modes excited in a magnetic insulator by pure spin current, Sci. Rep. **6**, 32781 (2016).

[11] D. A. Bozhko, A. A. Serga, P. Clausen, V. I. Vasyuchka, F. Heussner, G. A. Melkov, A. Pomyalov, V. S. L'vov, and B. Hillebrands, Supercurrent in a room-temperature Bose-Einstein magnon condensate, Nat. Phys. **12**, 1057 (2016).

[12] M. B. Jungfleisch, W. Zhang, J. Sklenar, J. Ding, W. Jiang, H. Chang, F. Y. Fradin, J. E. Pearson, J. B. Ketterson, V. Novosad, M. Wu, and A. Hoffmann, Large Spin-Wave Bullet in a Ferrimagnetic Insulator Driven by the Spin Hall Effect, Phys. Rev. Lett. **116**, 057601 (2016).

[13] K. An, K. S. Olsson, A. Weathers, S. Sullivan, X. Chen, X. X. Li, L. G. Marshall, X. Ma, N. Klimovich, J. Zhou, L. Shi, and X. X. Li, Magnons and Phonons Optically Driven out of Local Equilibrium in a Magnetic Insulator, Phys. Rev. Lett. **117**, 107202 (2016).

[14] M. Montazeri, P. Upadhyaya, M. C. Onbasli, G. Yu, K. L. Wong, M. Lang, Y. Fan, X. Li, P. Khalili Amiri, R. N. Schwartz, C. A. Ross, and K. L. Wang, Magneto-optical investigation of spin-orbit torques in metallic and insulating magnetic heterostructures, Nat. Commun. **6**, 8958 (2015).

[15] M. Weiler, M. Althammer, F. D. Czeschka, H. Huebl, M. S. Wagner, M. Opel, I.-M. Imort, G. Reiss, A. Thomas, R. Gross, and S. T. B. Goennenwein, Local Charge and Spin Currents in Magnetothermal Landscapes, Phys. Rev. Lett. **108**, 106602 (2012).

[16] Y. Kajiwara, K. Harii, S. Takahashi, J. Ohe, K. Uchida, M. Mizuguchi, H. Umezawa, H. Kawai, K. Ando, K. Takanashi, S. Maekawa, and E. Saitoh, Transmission of electrical signals by spin-wave interconversion in a magnetic insulator, Nature (London) **464**, 262 (2010).

[17] J. Xiao, G. E. W. Bauer, K. Uchida, E. Saitoh, and S. Maekawa, Theory of magnon-driven spin Seebeck effect, Phys. Rev. B **81**, 214418 (2010).

[18] S. M. Rezende, R. L. Rodríguez-Suárez, R. O. Cunha, A. R. Rodrigues, F. L. A. Machado, G. A. Fonseca Guerra, J. C. Lopez Ortiz, and A. Azevedo, Magnon spin-current theory for the longitudinal spin-Seebeck effect, Phys. Rev. B **89**, 014416 (2014).

[19] M. Schreier, A. Kamra, M. Weiler, J. Xiao, G. E. W. Bauer, R. Gross, and S. T. B. Goennenwein, Magnon, phonon, and electron temperature profiles and the spin Seebeck effect in magnetic insulator/normal metal hybrid structures, Phys. Rev. B **88**, 094410 (2013).

[20] K. Uchida, H. Adachi, T. Ota, H. Nakayama, S. Maekawa, and E. Saitoh, Observation of longitudinal spin-Seebeck effect in magnetic insulators, Appl. Phys. Lett. **97**, 172505 (2010).

[21] C. M. Jaworski, J. Yang, S. Mack, D. D. Awschalom, J. P. Heremans, and R. C. Myers, Observation of the spin-Seebeck effect in a ferromagnetic semiconductor, Nat. Mater. **9**, 898 (2010).

[22] J. Kimling, G.-M. Choi, J. T. Brangham, T. Matalla-Wagner, T. Huebner, T. Kuschel, F. Yang, and D. G. Cahill, Picosecond Spin Seebeck Effect, Phys. Rev. Lett. **118**, 057201 (2017).

[23] S. Hoffman, K. Sato, and Y. Tserkovnyak, Landau-Lifshitz theory of the longitudinal spin Seebeck effect, Phys. Rev. B **88**, 064408 (2013).

[24] A. von Bieren, F. Brandl, D. Grundler, and J.-P. Ansermet, Space- and time-resolved Seebeck and Nernst voltages in laser-heated permalloy/gold microstructures, Appl. Phys. Lett. **102**, 052408 (2013).

[25] J. M. Bartell, D. H. Ngai, Z. Leng, and G. D. Fuchs, Towards a table–top microscope for nanoscale magnetic imaging using picosecond thermal gradients, Nat. Commun. **6**, 8460 (2015).

[26] T. Miyasato, N. Abe, T. Fujii, A. Asamitsu, S. Onoda, Y. Onose, N. Nagaosa, and Y. Tokura, Crossover Behavior of

the Anomalous Hall Effect and Anomalous Nernst Effect in Itinerant Ferromagnets, Phys. Rev. Lett. **99**, 086602 (2007).

[27] N. Nagaosa, J. Sinova, S. Onoda, A. H. MacDonald, and N. P. Ong, Anomalous Hall effect, Rev. Mod. Phys. **82**, 1539 (2010).

[28] M. Schreier, F. Kramer, H. Huebl, S. Geprägs, R. Gross, S. T. B. Goennenwein, T. Noack, T. Langner, A. A. Serga, B. Hillebrands, and V. I. Vasyuchka, Spin Seebeck effect at microwave frequencies, Phys. Rev. B **93**, 224430 (2016).

[29] S. R. Etesami, L. Chotorlishvili, and J. Berakdar, Spectral characteristics of time resolved magnonic spin Seebeck effect, Appl. Phys. Lett. **107**, 132402 (2015).

[30] M. Agrawal, V. I. Vasyuchka, A. A. Serga, A. Kirihara, P. Pirro, T. Langner, M. B. Jungfleisch, A. V. Chumak, E. T. Papaioannou, and B. Hillebrands, Role of bulk-magnon transport in the temporal evolution of the longitudinal spin-Seebeck effect, Phys. Rev. B **89**, 224414 (2014).

[31] B. L. Giles, Z. Yang, J. S. Jamison, and R. C. Myers, Long-range pure magnon spin diffusion observed in a nonlocal spin-Seebeck geometry, Phys. Rev. B **92**, 224415 (2015).

[32] H. L. Wang, C. H. Du, Y. Pu, R. Adur, P. C. Hammel, and F. Y. Yang, Large spin pumping from epitaxial $Y_3Fe5_3O_{12}$ thin films to Pt and W layers, Phys. Rev. B **88**, 100406 (2013).

[33] H. L. Wang, C. H. Du, Y. Pu, R. Adur, P. C. Hammel, and F. Y. Yang, Scaling of Spin Hall Angle in 3*d*, 4*d*, and 5*d* Metals from $Y_3Fe_5O_{12}$/Metal Spin Pumping, Phys. Rev. Lett. **112**, 197201 (2014).

[34] J. T. Brangham, K.-Y. Meng, A. S. Yang, J. C. Gallagher, B. D. Esser, S. P. White, S. Yu, D. W. McComb, P. C. Hammel, and F. Yang, Thickness dependence of spin Hall angle of Au grown on $Y_3Fe_5O_{12}$ epitaxial films, Phys. Rev. B **94**, 054418 (2016).

[35] T. Kikkawa, K. Uchida, Y. Shiomi, Z. Qiu, D. Hou, D. Tian, H. Nakayama, X.-F. Jin, and E. Saitoh, Longitudinal Spin Seebeck Effect Free from the Proximity Nernst Effect, Phys. Rev. Lett. **110**, 067207 (2013).

[36] B. F. Miao, S. Y. Huang, D. Qu, and C. L. Chien, Absence of anomalous Nernst effect in spin Seebeck effect of Pt/YIG, AIP Adv. **6**, 015018 (2016).

[37] D. Ellsworth, L. Lu, J. Lan, H. Chang, P. Li, Z. Wang, J. Hu, B. Johnson, Y. Bian, J. Xiao, R. Wu, and M. Wu, Photo-spin-voltaic effect, Nat. Phys. **12**, 861 (2016).

[38] F. Guo, J. M. Bartell, D. H. Ngai, and G. D. Fuchs, Phase-Sensitive Imaging of Ferromagnetic Resonance Using Ultrafast Heat Pulses, Phys. Rev. Applied **4**, 044004 (2015).

[39] See Supplemental Material at http://link.aps.org/supplemental/10.1103/PhysRevApplied.7.044004 for details of the design and characterization of the magnetothermal microscope as well as discussion related to the determination of the temperature increase and the image analysis.

[40] J. H. Weaver, Optical properties of Rh, Pd, Ir, and Pt, Phys. Rev. B **11**, 1416 (1975).

[41] A. D. Rakić, A. B. Djurišić, J. M. Elazar, and M. L. Majewski, Optical properties of metallic films for vertical-cavity optoelectronic devices, Appl. Opt. **37**, 5271 (1998).

[42] *CRC Handbook of Chemistry and Physics*, 97th ed., edited by E. W. M. Haynes (CRC Press/Taylor & Francis, Boca Raton, FL, 2016).

[43] A. M. Hofmeister, Thermal diffusivity of garnets at high temperature, Phys. Chem. Miner. **33**, 45 (2006).

[44] A. E. Clark and R. E. Strakna, Elastic constants of single-crystal YIG, J. Appl. Phys. **32**, 1172 (1961).

[45] S. Wemple, S. Blank, J. Seman, and W. Biolsi, Optical properties of epitaxial iron garnet thin films, Phys. Rev. B **9**, 2134 (1974).

[46] D. L. Wood and K. Nassau, Optical properties of gadolinium gallium garnet, Appl. Opt. **29**, 3704 (1990).

[47] M. Schreier, T. Chiba, A. Niedermayr, J. Lotze, H. Huebl, S. Geprägs, S. Takahashi, G. E. W. Bauer, R. Gross, and S. T. B. Goennenwein, Current-induced spin torque resonance of a magnetic insulator, Phys. Rev. B **92**, 144411 (2015).

[48] T. Chiba, G. E. Bauer, and S. Takahashi, Current-Induced Spin-Torque Resonance of Magnetic Insulators, Phys. Rev. Applied **2**, 034003 (2014).

[49] J. Sklenar, W. Zhang, M. B. Jungfleisch, W. Jiang, H. Chang, J. E. Pearson, M. Wu, J. B. Ketterson, and A. Hoffmann, Driving and detecting ferromagnetic resonance in insulators with the spin Hall effect, Phys. Rev. B **92**, 174406 (2015).

[50] N. Vlietstra, J. Shan, V. Castel, B. J. van Wees, and J. Ben Youssef, Spin-Hall magnetoresistance in platinum on yttrium iron garnet: Dependence on platinum thickness and in-plane/out-of-plane magnetization, Phys. Rev. B **87**, 184421 (2013).

[51] M. Weiler, M. Althammer, M. Schreier, J. Lotze, M. Pernpeintner, S. Meyer, H. Huebl, R. Gross, A. Kamra, J. Xiao, Y.-T. Chen, H. Jiao, G. E. W. Bauer, and S. T. B. Goennenwein, Experimental Test of the Spin Mixing Interface Conductivity Concept, Phys. Rev. Lett. **111**, 176601 (2013).

[52] M. Althammer *et al.* Quantitative study of the spin Hall magnetoresistance in ferromagnetic insulator/normal metal hybrids, Phys. Rev. B **87**, 224401 (2013).

[53] N. Vlietstra, J. Shan, B. J. van Wees, M. Isasa, F. Casanova, and J. Ben Youssef, Simultaneous detection of the spin-Hall magnetoresistance and the spin-Seebeck effect in platinum and tantalum on yttrium iron garnet, Phys. Rev. B **90**, 174436 (2014).

[54] C. Hahn, G. de Loubens, O. Klein, M. Viret, V. V. Naletov, and J. Ben, Youssef, Comparative measurements of inverse spin Hall effects and magnetoresistance in YIG/Pt and YIG/Ta, Phys. Rev. B **87**, 174417 (2013).